Three-Dimensional Whole-Heart T_2 Mapping at 3T

Haiyan Ding,[1,2] Laura Fernandez-de-Manuel,[2,3] Michael Schär,[4,5] Karl H. Schuleri,[6] Henry Halperin,[6] Le He,[1] M. Muz Zviman,[6] Roy Beinart,[6,7] and Daniel A. Herzka[2]*

Purpose: Detecting variations in myocardial water content with T_2 mapping is superior to conventional T_2-weighted MRI since quantification enables direct observation of complicated pathology. Most commonly used T_2 mapping techniques are limited in achievable spatial and/or temporal resolution, both of which reduce accuracy due to partial-volume averaging and misregistration between images. The goal of this study was to validate a novel free breathing T_2 mapping sequence that overcomes these limitations.

Methods: The proposed technique was made insensitive to heart rate variability through the use of a saturation prepulse to reset magnetization every heartbeat. Respiratory navigator-gated, differentially T_2-weighted volumes were interleaved per heartbeat, guaranteeing registered images and robust voxel-by-voxel T_2 maps. Free breathing acquisitions removed limits on spatial resolution and allowed short diastolic windows. Accuracy was quantified with simulations and phantoms.

Results: Homogeneous three-dimensional (3D) T_2 maps were obtained from normal human subjects and swine. Normal human and swine left ventricular T_2 values were 42.3 ± 4.0 and 43.5 ± 4.3 ms, respectively. The T_2 value for edematous myocardium obtained from a swine model of acute myocardial infarction was 59.1 ± 7.1 ms.

Conclusion: Free-breathing accurate 3D T_2 mapping is feasible and may be applicable in myocardial assessment in lieu of current clinical black blood, T_2-weighted techniques. **Magn Reson Med 74:803–816, 2015. © 2014 Wiley Periodicals, Inc.**

Key words: cardiac magnetic resonance imaging; T_2 mapping; 3D; free breathing; T_2 relaxation time; relaxometry

INTRODUCTION

Myocardial edema is caused by increased water content and can be observed by a commensurate elevation in T_2 relaxation time. This relationship makes T_2 and T_2-weighted imaging very useful in cardiac MR. In particular, T_2-elevation has been documented in acute myocardial infarction, myocarditis, allograft rejection, and sarcoidosis, among other conditions (1–10).

Traditional black-blood spin echo-based T_2-weighted imaging (11) is limited by its innate sensitivity to motion, the contamination of the measured signal by contributions from stagnant, slow-moving blood, and by its requirement for subjective interpretation of images (12). As an alternative, quantitative T_2 mapping can provide accurate and reliable detection of edematous myocardial tissue by overcoming the limitations of qualitative T_2-weighted imaging, and this technique shows promise for application in clinical practice (13–19).

The most commonly used T_2 mapping techniques are limited by their achievable spatial resolution and sensitivity to motion, making accurate T_2 mapping a challenge. For example, previous attempts at T_2 mapping using multiple diastolic images with differential T_2 preparation rely on single-shot imaging, which results in limited resolution and is susceptible to errors in fitting from: 1) partial volume averaging, 2) misregistration of images due to broad diastolic imaging windows and poor breath-holding, and 3) T_1-induced signal variability resulting from the typical heart variability presented in patients with heart disease. Ultimately, breath-holding constrains total imaging time, limiting spatial resolution, total coverage, and making quantification susceptible to errors related to patient compliance (20).

In this study, we developed a free-breathing, three-dimensional (3D) T_2 mapping method based on the saturation-prepared, T_2-prepared (T_2 Prep) radiofrequency-spoiled gradient echo (SPGR) sequence, which achieves high spatial resolution T_2 maps with whole heart coverage. Compared with previous T_2 mapping methods, the presented sequence is 1) less dependent on field homogeneity (obtained by using SPGR and partial echo readout), 2) highly efficient (by utilizing all heartbeats for imaging and requiring no T_1 recovery time), 3) motion compensated (via respiratory navigators), 4) insensitive to heart rate variation (by using a "reset" nonselective saturation prepulse), and 5) intrinsically spatially registered by interleaving volumes with different T_2 Prep. The 3D acquisition improved both through-plane motion compensation and signal-to-noise ratio (SNR) compared with previous techniques (21).

We quantify the accuracy of the technique with simulations and measurement in phantoms, and demonstrate 3D whole-heart T_2 maps in normal human subjects,

[1]Center for Biomedical Imaging Research, Department of Biomedical Engineering, Tsinghua University, Beijing, People's Republic of China.

[2]Department of Biomedical Engineering, Johns Hopkins School of Medicine, Baltimore, Maryland, USA.

[3]Biomedical Image Technologies Laboratory, ETSI Telecomunicación, Universidad Politécnica de Madrid, and CIBER-BBN, Madrid, Spain.

[4]Russell H. Morgan Department of Radiology and Radiological Science, Johns Hopkins School of Medicine, Baltimore, Maryland, USA.

[5]Philips Healthcare, Cleveland, Ohio, USA.

[6]Department of Medicine, Cardiology, Johns Hopkins School of Medicine, Baltimore, Maryland, USA.

[7]Heart Institute, Sheba Medical Center, Tel Aviv University, Ramat Gan, Israel.

Grant sponsor: American Heart Association; Grant number: AHA-11SDG5280025; Grant sponsor: The Tsinghua University–Johns Hopkins University Biomedical Engineering joint center exchange program.

*Correspondence to: Daniel A. Herzka, 720 Rutland Avenue, 726 Ross Building, Baltimore, MD 21205. E-mail: daniel.herzka@jhu.edu

Received 23 June 2014; revised 23 August 2014; accepted 25 August 2014
DOI 10.1002/mrm.25458
Published online 19 September 2014 in Wiley Online Library (wileyonlinelibrary.com).

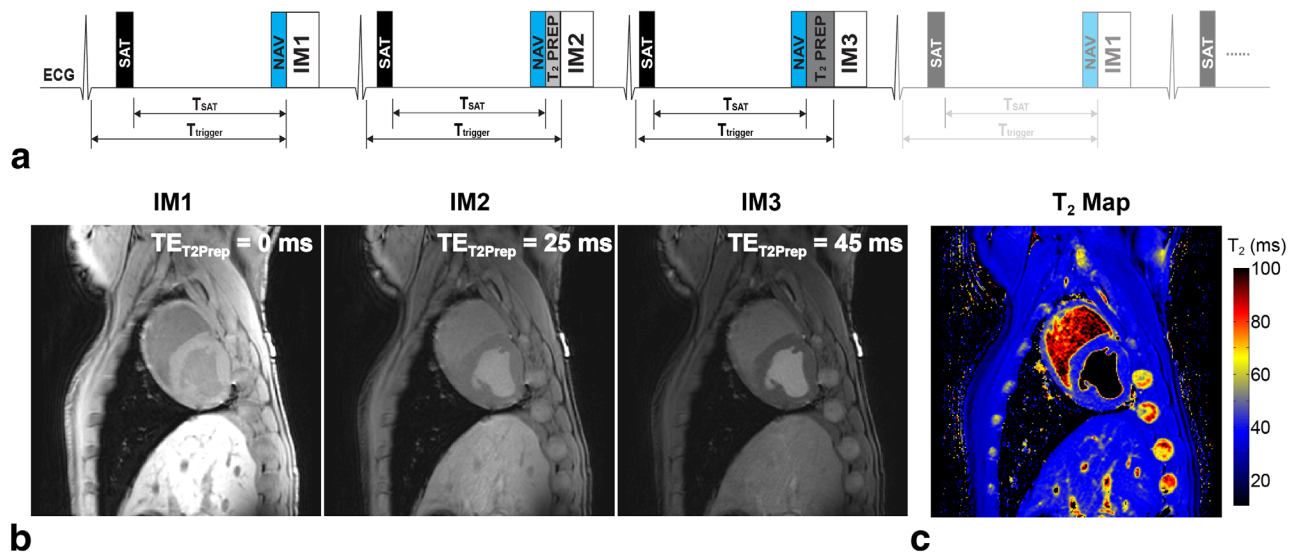

FIG. 1. **a**: Pulse sequence diagram for the free breathing 3D T_2 mapping sequence. Three or more differentially T_2-weighted volumes were acquired in an interleaved fashion. Each volume was respiratory navigator gated, ensuring coregistered images. A SAT pulse was applied at the start of every heartbeat to reduce variations in signal intensities. To prevent changing heart rates from affecting the degree of T_1-weighting in the images, the T_{SAT} (SAT delay, duration between SAT and T_2 Prep) was kept constant even when the $T_{trigger}$ (trigger delay, imaging delay after ECG R wave is detected) was allowed to change to maintain imaging during diastole in the presence of heart rate variability. The same navigator template was used for detection of motion across all volumes, ensuring coregistration. If a given heartbeat was rejected due to respiratory motion, data were reacquired immediately until an appropriate level of motion was achieved before proceeding to the next volume's data. **b:** Sample images from three acquired 3D volumes yielded voxel-by-voxel 3D T_2 maps (**c**).

normal swine, and in a swine model of myocardial infarction at 3T.

METHODS

All imaging studies were performed on a 3 T MR system (Achieva TX, Philips Healthcare, Best, Netherlands). Cardiac studies used a 32-channel phased array (InVivo, Gainesville, Florida, USA) and phantom studies used an eight-channel head coil. All animal studies were approved by the Institutional Animal Care and Use Committee. The human study was approved by the local Institutional Review Board. Written informed consent was obtained from all subjects. Simulations, image processing, and statistical analysis were implemented in MATLAB (MathWorks, Natick, Massachusetts, USA).

Pulse Sequence

The proposed free-breathing 3D T_2 mapping method uses multiple differentially T_2-weighted volumes to yield voxel-by-voxel parametric maps. The sequence combines a saturation prepulse (SAT), respiratory navigators (NAVs), and T_2 Prep (22) as shown in Figure 1A. The volumes were T_2-prepared using adiabatic T_2 Prep (23) and were acquired in an interleaved manner over several heartbeats during diastole. The SAT pulse was applied after the electrocardiographic (ECG) trigger at a fixed predelay to the imaging window (T_{SAT}) and was designed to reset the magnetization at the start of each heartbeat. The SAT pulse was a nonselective 90° saturation pulse with a time-bandwidth product of 8.352. This removed heart rate dependency during the scan and allowed for imaging every heartbeat.

The SAT was applied as soon as possible after the ECG trigger to ensure maximal magnetization recovery before imaging. However, because the timing of the imaging window was adjusted on a per-heartbeat basis to ensure diastolic imaging (24), the SAT timing was also adjusted to maintain a constant delay to the onset of imaging. Hence, a small delay window was used to ensure the correct timing. Different T_2 weightings were achieved with adiabatic T_2 Prep with different echo times ($TE_{T2\,Prep}$), including one volume with no T_2 Prep and preserved timing (Fig. 1B). The non–T_2-prepared volume (i.e., $TE_{T2\,Prep} = 0$ ms) had the highest SNR and was used to increase image quality. The minimum $TE_{T2\,Prep}$ using the standard adiabatic pulses was $TE_{T2\,Prep} =$ 25 ms. The maximum used $TE_{T2\,Prep}$ was 45 ms, which is the estimated value of normal myocardium at 3 T. Higher $TE_{T2\,Prep}$ resulted in artifacts from residual phase resulting in nonuniform magnetization.

Free-breathing acquisitions with respiratory motion compensation were achieved by using a pencil beam navigator placed at the lung–liver interface of the right hemidiaphragm (25). The NAV was sampled before T_2 Prep to ensure NAV signal similarity across volumes. The same NAV template was used for detection of motion across all volumes, ensuring coregistration. Executing T_2 Prep after the NAV also resulted in minimization of the time between T_2 weighting and imaging, leading to more correct contrast. The use of free-breathing acquisitions made high-resolution, multivolume 3D scans with whole heart coverage possible.

Data for the differentially T_2-weighted volumes was acquired in an interleaved fashion. Interleaving was used to avoid misregistration, which could present with

current single-shot relaxometry techniques and interfere with accurate voxel-by-voxel parametric fitting, or require significant motion correction on a per-frame basis (10,13,26,27). One heartbeat's worth of phase encoding steps was acquired for all differentially T_2-weighted volumes before proceeding to the next set of phase encoding steps. If a given heartbeat was rejected due to respiratory motion, data were reacquired immediately until an appropriate level of motion was achieved before proceeding to the next volume's data (Fig. 1A). The interleaving of the acquisition of the differentially T_2-weighted volumes resulted in intrinsic spatial alignment with reduced motion sensitivity and minimized spatial misregistration in the T_2-weighted volumes, as any variation in the underlying motion patterns affected all volumes equally (28,29).

General Acquisition Parameters

The relevant acquisition parameters are summarized in Table 1. Three-dimensional Cartesian sampling T_2 mapping was performed with a 5/8 fractional readout gradient echo (SPGR) using elliptical centric view ordering (30) in the k_y-k_z plane with 78% coverage, which was reconstructed on the scanner by dual phase partial echo method (31). The acquisition window in diastasis was kept to <100 ms to minimize cardiac motion (32). Both ROI-specific B_1+ and B_0 shimming (33,34) were performed before the 3D imaging to compensate for any field inhomogeneities.

Simulations

T_1 recovery during T_{SAT} is the primary quantity that can affect the estimation of T_2 values, as different heart rates can lead to variable trigger delays for imaging as well as T_{SAT}. This consequently changes the signal intensity at the onset of imaging (Appendix 1). In the simulation, T_{SAT} was defined as the longest duration between SAT and imaging module by excluding all the preparation. The timing for mid-diastolic imaging was calculated using an empirical relationship between heart rate and the delay to diastasis (Appendix 2) (24,35).

Simulations were written to explore the dependency of the magnitude of the magnetization available for imaging post T_2 Prep on heart rate, assuming middiastolic imaging. The Bloch equations were used to determine the magnetization as functions of tissue T_1 (800–1400 ms), T_2 (20–100 ms), $TE_{T2\,Prep}$ (0–100 ms), and heart rate (50–120 bpm). Normal myocardium with T_1 (1200 ms) and T_2 (40 ms) was simulated to investigate the signal intensity behavior for different heart rate and T_2 Prep (36).

Phantom Studies

Gel phantom studies were performed to validate the proposed sequence. Phantoms (n = 8) were prepared using Gd-DTPA (Magnevist, Berlex) and 1.65%–4.5% Agarose by weight (Sigma-Aldrich) to approximate T_1 and T_2 values near those of normal myocardium at 3 T. Reference T_1 values were measured using the IR prepared T_1-weighted sequence (37) with TI ranging from 30 ms to 3530 ms. Reference T_2 values were measured with a 3D single-echo spin echo sequence with eight TE values ranging from 7.5 to 60.0 ms and with a TR of 10 s for complete magnetization recovery.

To determine the accuracy of the proposed T_2 mapping technique, nine volumes were imaged with $TE_{T2\,Prep}$ values in the range {0, 25, 30, ... 60} ms and a step-size of 5 ms using a simulated heart rate of 60 bpm and a 522-ms T_{SAT} to mimic diastole imaging. Imaging was performed with a 3D SPGR sequence using TR/TE 1.9/0.75 ms, a 5/8 fractional readout, an acquisition window of 28.0 ms, and 15 readouts per heartbeat. A similar length readout train was used in the in vivo study. Other imaging parameters were: spatial resolution $2.0 \times 2.0 \times 8.0$ mm^3 reconstructed to $1.0 \times 1.0 \times 8.0$ mm^3. Neither fat suppression nor navigator prepulse was used.

To explore the sensitivity of the calculated T_2 values to heart rate or T_1 recovery, eight additional T_2 mapping scans with T_{SAT} ranging {272, ... 672} ms with a step size of 50 ms were acquired; these corresponded to heart rates {55, ... 140} bpm for middiastole imaging. In all, nine T_2 maps were used to investigate T_2 estimation error as a function of heart rate.

Both T_2 maps from spin echo and the T_2 mapping sequences were fit using the same linear regression method (Appendix 1). Only the central slice of the T_2 map was used for further quantitative analysis to avoid imperfect slice profile effects. The same ROI with 200 pixels was drawn on each phantom on the T_2 maps. Correlation between the T_2 values from the T_2 mapping and that from spin echo was calculated by pixel-by-pixel linear regression.

To determine the effects of the number of $TE_{T2\,Prep}$ values for the in vivo study, three values of $TE_{T2\,Prep}$ {0, 25, 45} ms and four values of $TE_{T2\,Prep}$ {0, 25, 35, 45} ms were tested for T_2 fitting accuracy. The relative error was defined as the difference between T_2 estimated from T_2 mapping and the T_2 obtained from the spin echo.

Normal Human Subjects Studies

Twelve normal subjects without known cardiovascular dysfunction (n = 6 females, n = 6 males) were enrolled and evenly grouped by two imaging resolutions (low resolution, $2 \times 2 \times 8$ mm^3; high resolution, $1.25 \times 1.25 \times 5$ mm^3) with a 50:50 sex distribution in each group. The ages for the low-resolution and high-resolution groups were 28.3 ± 4.5 y and 28.7 ± 6.7 y, respectively. Images were acquired during diastasis as identified from balanced steady-state free precession (bSSFP) cine imaging. Three or four differentially T_2-weighted volumes were acquired without using any parallel imaging.

Animal Studies

Normal swine (n = 3, 35–50 kg) and a swine model of reperfused acute myocardial infarction (MI) (n = 6, 35–50 kg) were imaged. Acute MI was created using a 120-min balloon occlusion distal to the second diagonal branch of the left anterior descending coronary artery with a balloon angioplasty catheter under fluoroscopic guidance (38). Occlusion and restoration of flow in the artery after reperfusion were confirmed via angiography. Imaging took place 2 to 3 days after MI when the animal achieved a stable physiological state. Animals were mechanically ventilated with 1.5%–2% isoflurane during imaging.

Table 1
Imaging Parameters for the In Vivo Studies

Parameter	3D free breathing T_2 mapping			3D free breathing PSIR LGE	2D BB T_2-STIR
	Human, Low-Resolution	Human, High-Resolution	Swine	Swine	Swine
Imaging sequence	Gradient echo	Gradient echo	Gradient echo	Gradient echo	Spin echo
T_2 Prep echo time, ms	0, 25, 45	0, 25, 35, 45	0, 25, 45	—	-
Readout TR/TE, ms	3.3/1.0	4.1/1.2	4/1.2	5.5/2.7	2 × RR/40
Readouts per heartbeat, mean ± standard deviation (range)	22 ± 4 (18–26)	21 ± 3 (18–26)	15 ± 3 (12–18)	14 ± 2 (12–16)	10
Temporal resolution/acquisition window, ms, mean ± standard deviation (range)	73.1 ± 13.6 (65.3–85.8)	85.5 ± 11.0 (73.7–105.4)	62 ± 12 (48–73)	78 ± 9 (66–86)	100.8 ± 0.2 (100.7–101.2)
Flip angle	18°	18°	18°	18°	90°
Acquired voxel size, mm^3	2.0 × 2.0 × 8.0	1.25 × 1.25 × 5.0	1.25 × 1.25 × 5.0	1.0 × 1.27 × 3.0	1.25 × 1.28 × 5.0
Reconstructed voxel size, mm^3	0.98 × 0.98 × 4.0	0.98 × 0.98 × 2.5	0.98 × 0.98 × 2.5	0.74 × 0.74 × 1.5	0.98 × 0.98 × 5.0
Parallel acquisition (technique/acceleration)	—	—	—	SENSE/R = 2	—
Field of view, mm^3[a]	270 × 220 × 82	267 × 234 × 90	236 × 220 × 80	239 × 215 × 81	246 × 226 × 75
Acquisition matrix[a]	134 × 110 × 13	214 × 186 × 23	189 × 176 × 21	240 × 163 × 35	197 × 177 × 15
Heart rate, bpm, mean ± standard deviation	68 ± 7	71 ± 11	77 ± 10	78 ± 6	77 ± 11
Prescribed scan time, s, mean ± standard deviation	133 ± 35	535 ± 116	427 ± 153	347 ± 114	418 ± 146 (~33 s breath-hold/slice)
Respiratory gating efficiency, %	30–60	40–60	40–50	35–45	—

PSIR, phase sensitive inversion recovery; TE, echo time; TR, pulse repetition time.
[a]Average of all cases, where (R × P × S) represent readout, phase, and slice encodings. Slice encoding included a standard oversampling ratio 1.28 and zero padding into the prescribed slice thickness. Use of an elliptical window in the k_y-k_z plane reduced the total number of phase encodings acquired by 22%.

Breath-hold black blood T_2 short tau inversion recovery (BB T_2-STIR) (11) and the proposed free-breathing T_2 mapping sequences were performed before contrast injection. Late gadolinium-enhanced imaging (LGE) with an independently respiratory NAV-gated 3D phase sensitive inversion recovery (39,40) was performed ~20 min after intravenous injection of contrast agent (0.2 mmol/kg, Magnevist, Berlex).

Image Processing and Statistical Analysis

Pixel-by-pixel T_2 maps were fit offline using a linear regression method described in Appendix 1. A pixel was considered to have a successful fit if $R^2 > 0.9$. As shown in Figure 2, the left ventricle (LV) was manually segmented slice by slice on T_2 maps from in vivo studies, with papillary muscle and epi-/endocardial boundaries excluded to avoid partial volume effects (Seg3D, 2011, University of Utah) (41) (Fig. 2B). Two observers agreed upon the segmentation. Long axis four-chamber views were generated by reformatting the 3D dataset (Fig. 2C). No registration between scans was necessary, and no interpolation other than zero padding was used. The T_2 fitting process was finished in MATLAB in <10 s for the four whole heart, high-resolution, 4 T_2-weighted volumes using a standard laptop (2.7 GHz Intel Core i7 processor, 16GB 1600 MHz DDR3 memory).

For the display of T_2 maps, a separate color scale was designed and included blue, yellow, and red separated by linear gradients on the RGB color model. Pixels with T_2 values <15 ms or >100 ms as well as pixels with unsuccessful fits ($R^2 < 0.9$) were displayed using black. Using this color scale, normal myocardium was centered on pure blue, mildly edematous myocardium appeared yellow, and severely edematous myocardium appeared orange or red. One of the aims of this color scale was to avoid the perceptual issues associated with the rainbow or "jet" color scales that are commonly used to display parametric maps (42). Furthermore, values of T_2 outside the accurate range of the presented technique were not assigned the equivalent color despite having a successful fit. No additional masking was applied to the maps.

To visualize the 3D whole heart T_2 maps, all data were mapped onto bull's-eye plots that mapped the whole heart onto a two-dimensional (2D) disk after averaging in the radial direction per slice. The orientation of the AHA 17-segment model was used (43), but the high-resolution scans permitted more densely sampled plots spanning the LV with 90 radial segments per slice and with up to 26 slices in swine, and 18 or 32 slices in humans, depending on the imaging resolution (Fig. 2D). The most apical slices and upper basal slices were excluded to avoid partial volume effects. T_2 homogeneity and distribution over the LV was further evaluated via histogram analysis (Fig. 2E) and measuring the mean (μ) ± standard deviation (σ) for each short axis slice (Fig. 2F). In the acute MI swine, the average T_2 of edema was measured based on the area with T_2 above the average myocardial T_2 in normal swine plus 2σ. Note that the reference value used in the determination of edema came from the normal swine group.

The coefficient of variation (CV, the standard deviation of the differences divided by the mean) of each short

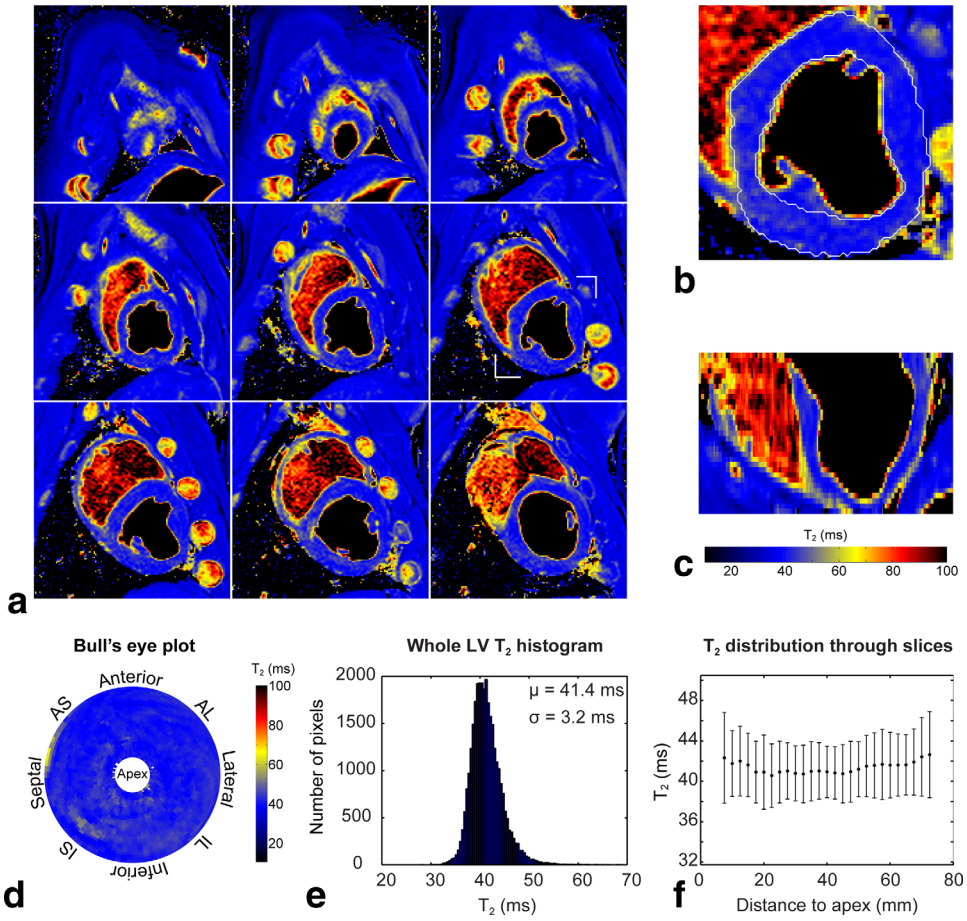

FIG. 2. **a, b**: Sample 3D T_2 maps (a) with magnification (b) and LV manually segmented white contours. **c:** The 3D nature of the acquisition allows for easy data reformatting in other orientations such as the long axis view. **d, e:** The 3D T_2 maps are represented in 2D as Bull's-eye plots (d) or via histogram of T_2 (e). **f:** Single short axis slice T_2 mean value (μ) and standard deviation (σ) distribution aids further visualization. AL, anterolateral; AS, anteroseptal; IL, inferolateral; IS, inferoseptal.

axis slice; averaged results from apical, midcavity, and basal slabs; and short axis radial segments were also calculated for further variability evaluation. The mean T_2 value and standard deviation were compared with previous reports from the literature. Statistical analysis of the differences in T_2 values between normal human subjects, normal swine, acute MI swine, and edema in acute MI swine was performed using an unpaired, two-tailed Student's t test (or Welch's t test) with a significance level of $\alpha = 0.05$. Analysis of variance was used to test the differences among the apical, midcavity, and basal slabs of all subjects from each group.

RESULTS

Simulations

Long $TE_{T2\,Prep}$ led to significant T_2 decay with the corresponding signal loss (Fig. 3). Given the constant noise level, image quality degraded the most when heart rate was high and $TE_{T2\,Prep}$ was long. The application of T_2 Prep with longer echo time led to significant signal reduction, implying that images acquired with longer $TE_{T2\,Prep}$ values contributed disproportionately to errors in T_2 measurements. As expected, T_2 Prep and heart rate had a strong influence on available signal. Sensitivity to variations in T_1 was low, as shown by the relatively slow signal change across different T_1 values.

Phantom Studies

Excellent correlations for the T_2 values typically observed in myocardium were obtained for all three $TE_{T2\,Prep}$ combinations, with little residual ($R^2 > 0.99$) and a regression slope >0.97 (Fig. 4A–C). The comparison between the three, four, and nine $TE_{T2\,Prep}$ combinations showed there were only slight differences in the values of their regression intercepts and regression slopes.

The difference in T_2 as measured by T_2 mapping or by single-echo spin echo (Fig. 4D–F) showed that the overall error was <4 ms, spanning the simulated heart rate range of 55–130 bpm. Samples with 41 ms $< T_2 <$ 71 ms showed consistent behavior in error. The phantoms with lowest or highest tested T_2 values (29/84 ms) had more variable error and presented decreased consistency among measurements from different $TE_{T2\,Prep}$ combinations.

The CV of T_2 from T_2 mapping decreased as the number of $TE_{T2\,Prep}$ volumes used in the measurement increased, reflecting an increased fidelity from better fits (Fig 4G–I). All samples except that with the longest T_2 value (84 ms) had a CV of <5%. More measurement

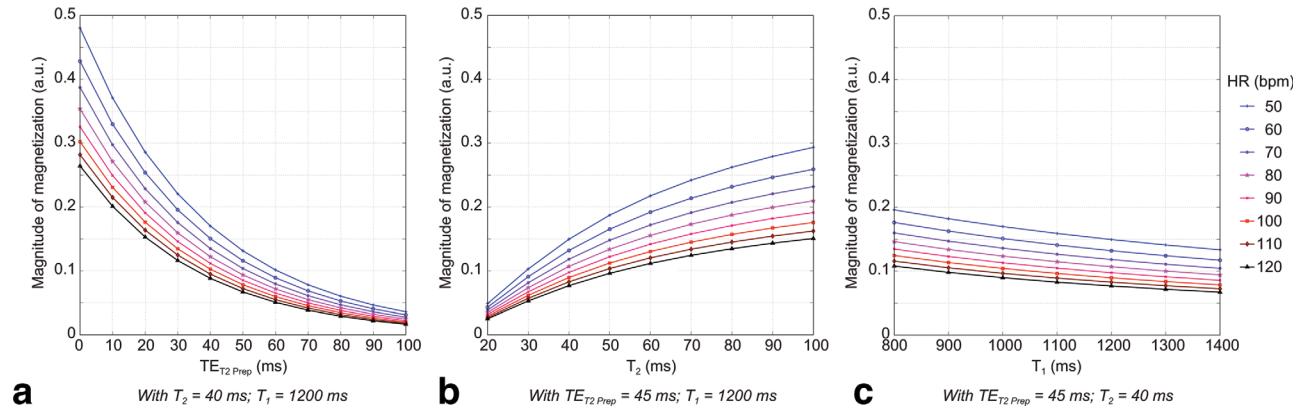

FIG. 3. Results from simulations show that the available magnitude of magnetization varies with T_2, $TE_{T2\,Prep}$, and heart rate for middiastolic imaging. **a:** Available magnetization over different $TE_{T2\,Prep}$ and heart rates at normal myocardial tissue T_1 (1200 ms) and T_2 (40 ms). **b:** Available magnetization over different T_2 species and heart rates at fixed $TE_{T2\,Prep}$ (45 ms) and T_1 (1200 ms). **c:** Available magnetization over different T_1 species and heart rates at fixed $TE_{T2\,Prep}$ (45 ms) and T_2 (40 ms).

volumes with different $TE_{T2\,Prep}$ values helped decrease the CV down to <2% for heart rate < 120 bpm when T_2 was <71 ms (Fig 4I). Measurements made with three or four volumes were quite similar, achieving CV < 4% for heart rate < 120 bpm. The comparable performance observed when using measurements derived from three or four $TE_{T2\,Prep}$ values implies that three volumes may be sufficient for the desired T_2 measurement accuracy for the signal-to-noise levels achieved in this setting and are therefore suitable for use in in vivo acquisitions.

Normal Human Subject Studies

The proposed 3D free-breathing T_2 mapping sequence was applied in all human subjects successfully with respiratory gating efficiency between 30% and 60%. The average prescribed scan time was 133 ± 35 s and 535 ± 116 s for the three low-resolution and four high-resolution T_2-prepared volumes, respectively. Figure 5 demonstrates the representative short axis T_2 maps at two imaging resolutions ($2 \times 2 \times 8$ mm^3 and $1.25 \times 1.25 \times 5$ mm^3) from one subject. T_2 was homogeneously distributed over the whole LV as shown by the histograms of T_2 over the whole LV wall. The lower-resolution T_2 map exhibited more partial volume averaging, as evidenced by the increased spread of the distributions.

The average T_2 values over the whole LV were 41.3 ± 5.0 ms and 42.3 ± 4.0 ms for the low-resolution and high-resolution groups, respectively. The corresponding average coefficients of variation for the two groups were 12% and 9%. Note that the T_2 maps produced pixel-by-pixel fits with an average R^2 of 0.99 ± 0.01. No significant difference was found between T_2 as measured from high- or low-resolution maps (unpaired Student's *t* test). The measured T_2 of normal human myocardium was consistent with values reported in the literature (10,36,44,45).

Animal Studies

Figure 6 demonstrates the comparison of BB T_2-STIR images, T_2 maps, and LGE images from one normal swine and two animals imaged in the acute stages of MI. The T_2 maps displayed consistent image quality in all cases, whereas the quality of BB T_2-STIR images varied significantly.

The normal swine (case 1) displayed homogeneous T_2 values (41.9 ± 4.1 ms) throughout the whole LV (Fig. 6A), and the T_2 values were very close to those obtained in normal human subjects. The edematous area in the acute MI swine could be identified in the T_2 maps by the yellow areas (Fig. 6B,C). The edema seen in case 2 was colocalized with the area of hyperintensity in the LGE images, but the territory with hyperintense T_2 exceeded that demarcated by LGE. The large T_2 elevation (51.8 ± 10.7 ms) found in case 3 (Fig. 6C) represented an entire edematous ventricle, likely due to repeated defibrillation during MI induction and reperfusion in this animal. Similarly, overall T_2 elevation in an acute MI patient has been reported previously (44). In addition to global edema resulting from defibrillation, Figure 6C displays an area of decreased T_2 in the septal wall that is well colocalized with microvascular obstruction as identified on the LGE image, and a hypointense region in the BB T_2-STIR image. This region was hypothesized to correspond to hemorrhage related to reperfusion injury, which is typical in this model of MI and in humans (46) and results from the by-products of the degradation of blood, in turn leading to a decrease in T_2 superimposed on the increase in T_2 due to edema (47,48).

In comparison, BB T_2-STIR suffers from signal loss due to motion and signal nonuniformity due to variable surface coil sensitivity. The technique fails to clearly demarcate the edematous regions due to signal contamination by stagnant blood at the endocardium. Additionally, in cases with global edema, there is no normal tissue that can be used as a reference, making it difficult to accurately quantify or segment the region of injury.

Figure 7 shows representative T_2 maps and their T_2 distribution from case 2 in Figure 6. The map has an acquired resolution of $1.25 \times 1.25 \times 5.0$ mm^3 interpolated into $0.98 \times 0.98 \times 2.5$ mm^3 with a field of view of $250 \times 240 \times 90$ mm^3. The scan time was 10:16 min for

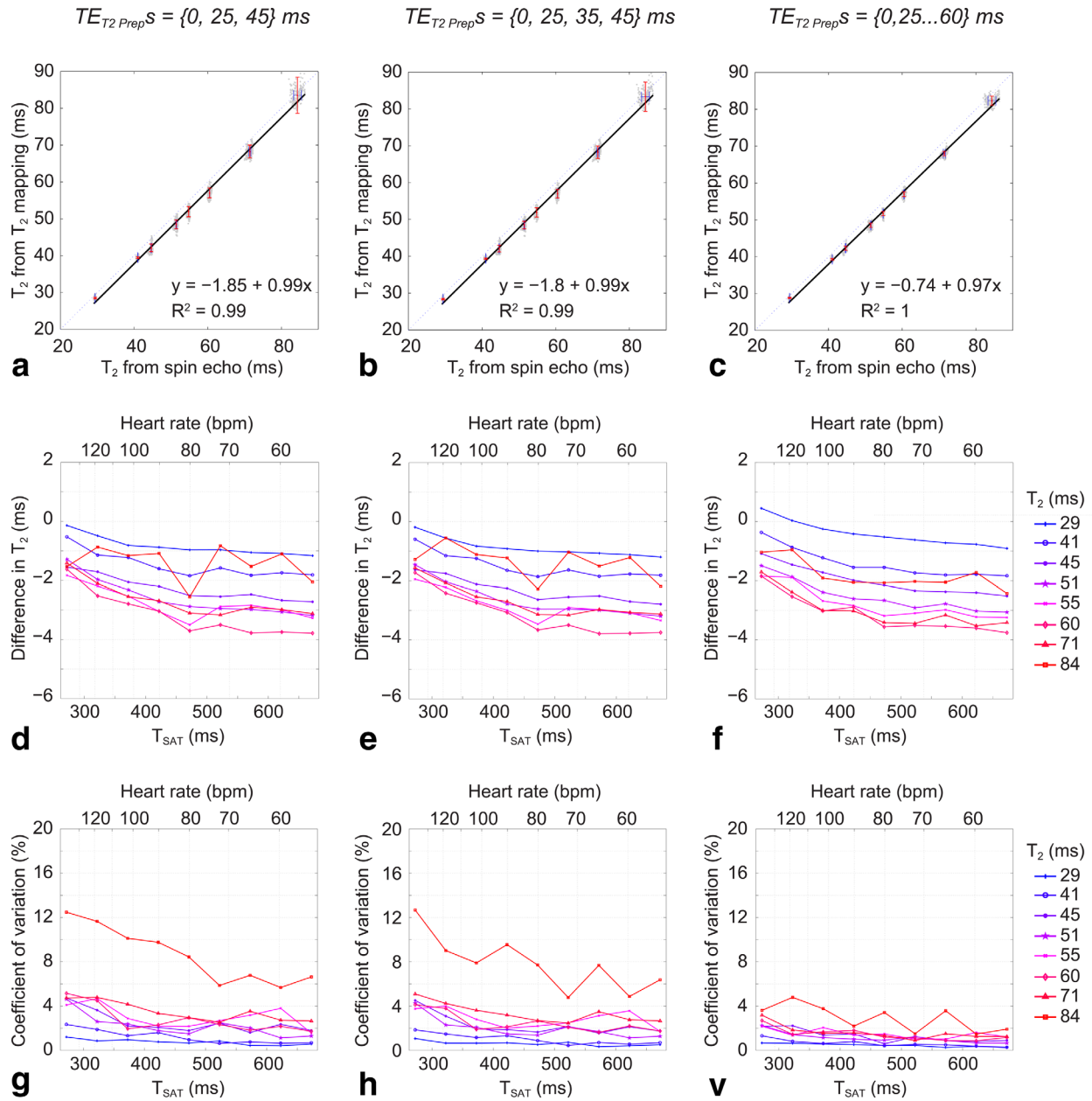

FIG. 4. Correlation of the T_2 values as measured in gel phantoms using single-echo spin echo and the proposed T_2 mapping (**a–c**), relative error as the difference in T_2 between measurements with T_2 mapping and spin echo (**d–f**) and the corresponding coefficient of variation on T_2 from T_2 mapping (**g–i**). The columns are the comparison among three, four, and nine $TE_{T2\,Prep}$ combinations. T_2 values in milliseconds for each phantom are shown in the legend. Longitudinal red and transversal blue bars in panels A–C represent the standard deviation of T_2 measurement from T_2 mapping and spin echo, respectively. The dotted blue line represents the identity. T_{SAT} is the delay duration from SAT prepulse to imaging session. Heart rate was calculated from empirical equation (Appendix 2), which matched the corresponding T_{SAT}.

three $TE_{T2\,Prep}$ volumes of this heart. The average T_2 value over the LV was 48.4 ± 9.1 ms. The area of edema extends from the apex to the midcavity level, as is apparent from the bull's-eye plot (Fig. 7D), and which can also be appreciated from the reformatted long axis view at the septal wall (Fig. 7C). The mean T_2 value and corresponding standard deviation of each slice is shown in Figure 7F. Obvious T_2 elevation with much bigger dynamic fluctuation occurs on slices from the apex to the middle of cavity. T_2 values revert back to normal for the basal slices.

Statistics

Figure 8 shows the quantitative comparison of the mean T_2 values in normal human subjects from both low- and high-resolution maps, the two animal groups without or with acute MI, and subgroup with edematous areas in acute MI animal. There was no statistical difference between the two measurements in normal subjects, nor between the normal human subjects and the normal swine. The T_2 values with $\mu \pm \sigma$ (fitting success rate, %) of the five groups were 41.3 ± 5.0 (99.5%), 42.3 ± 4.0 (99.8%),

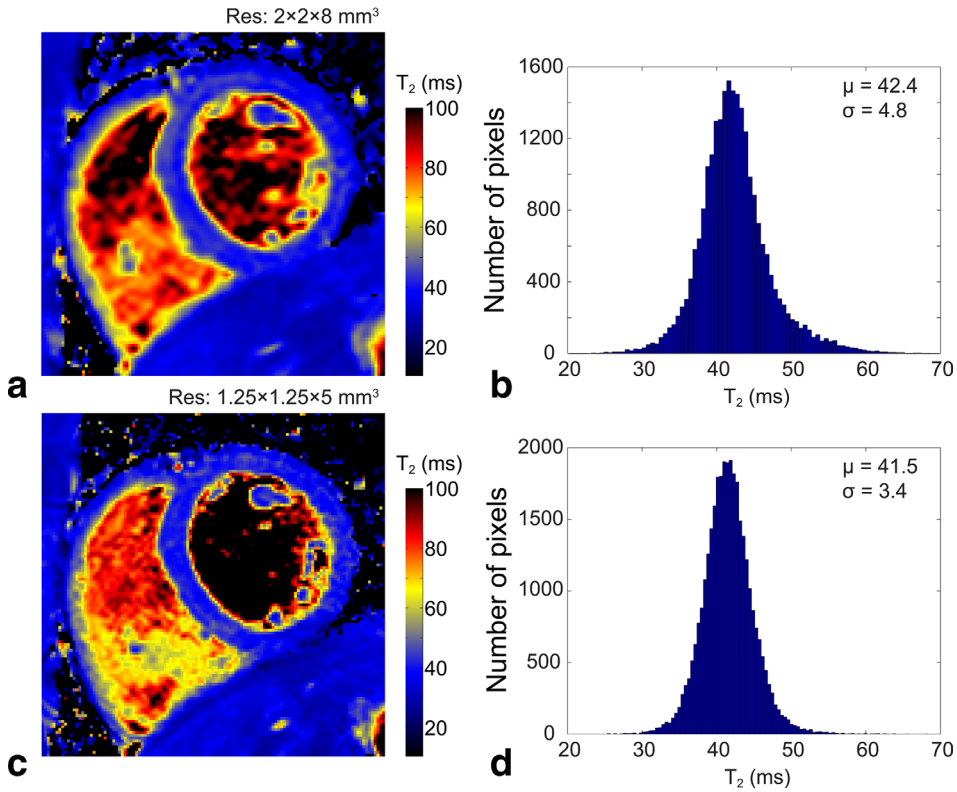

FIG. 5. Representative short axis T_2 maps of a normal human subject at different imaging resolution (**a**, **c**) and the associated whole LV T_2 value histograms (**b**, **d**). The 4-$TE_{T2\ Prep}$ volume high-resolution scan duration was 11:21 min and the 3-volume low-resolution scan duration was 3:47 min. No parallel imaging or other subsampling strategies were used. μ, mean; σ, standard deviation.

43.5 ± 4.3 (99.8%), 50.8 ± 8.6 (99.7%), and 59.1 ± 7.1 ms. For the acute MI swine, the average T_2 for the whole LV included both edematous and normal myocardium. After using the T_2 for normal myocardium determined from the normal swine group, the edematous tissue was separated, and the average T_2 for that tissue was determined (Fig. 9, rightmost group). Hence, no "normal" ROI was required in the acute MI swine for edema segmentation.

A single case of low-resolution imaging in normal subjects presented increased T_2 relative to the rest of the cohort. This may be a reflection of individual variability among subjects concordance with previous studies (13,17,36). The measure of average T_2 through the whole LV in animals with MI had a larger standard deviation as expected from the inclusion of edematous and normal tissue, as well as suspected hemorrhage ($P \ll 0.0001$). Despite the averaging across tissues, a significant difference ($P = 0.03$) was observed between the normal and the infarcted swine groups. As expected, a highly significant difference ($P \ll 0.0001$) was observed between the normal and the edematous areas in acute MI swine groups.

To examine the homogeneity of T_2 throughout the whole LV, all short axis T_2 maps for all the normal hearts were evenly grouped into three slabs corresponding to apical, midcavity, and basal myocardium and further partitioned into eight radial segments (Fig. 9). Both the high-resolution human and swine groups showed decreased T_2 variations among those segments in comparison with those of the low-resolution human group. The mean, standard deviation, and range for the apical, mid, and basal slabs obtained from the human high-resolution maps were 42.5 ± 2.3 (41.8–43.2), 42.4 ± 1.9 (41.1–44.0), and 42.3 ± 2.5 (41.1–43.8) ms, respectively. For the low-resolution T_2 maps, the comparable values for the three slabs were 43.1 ± 3.0 (41.5–44.7), 43.3 ± 3.3 (41.4–45.6), and 43.2 ± 3.7 (41.4–45.8) ms, respectively. Analysis of variance for the two human groups indicated no significant differences between the slabs: $P = 0.91$ and $P = 0.95$ for high- and low-resolution acquisitions, respectively. Though no significant difference in T_2 was found among the three slabs, both the standard deviations and the CVs over the 24 segments were decreased in higher-resolution acquisitions relative to the lower-resolution acquisitions (standard deviation = 0.83 and 1.36 ms, respectively; CV = 2.0% and 3.1%, respectively). These differences are most likely due to more obvious partial volume effects resulting from bigger voxels, an effect that is more pronounced in the apical regions of the heart.

DISCUSSION

This study demonstrates a novel 3D, free-breathing, T_2 mapping technique featuring heart rate insensitivity and high scan efficiency. The intrinsically coregistered acquisition on multiple differentially T_2-weighted volumes yielding a voxel-by-voxel T_2 map achieved accurate high-resolution, whole heart T_2 maps ($1.25 \times 1.25 \times 5$ mm^3). In phantoms, the proposed T_2 mapping sequence achieved excellent accuracy with linear regression $R^2 = 0.99$ against standard spin echo.

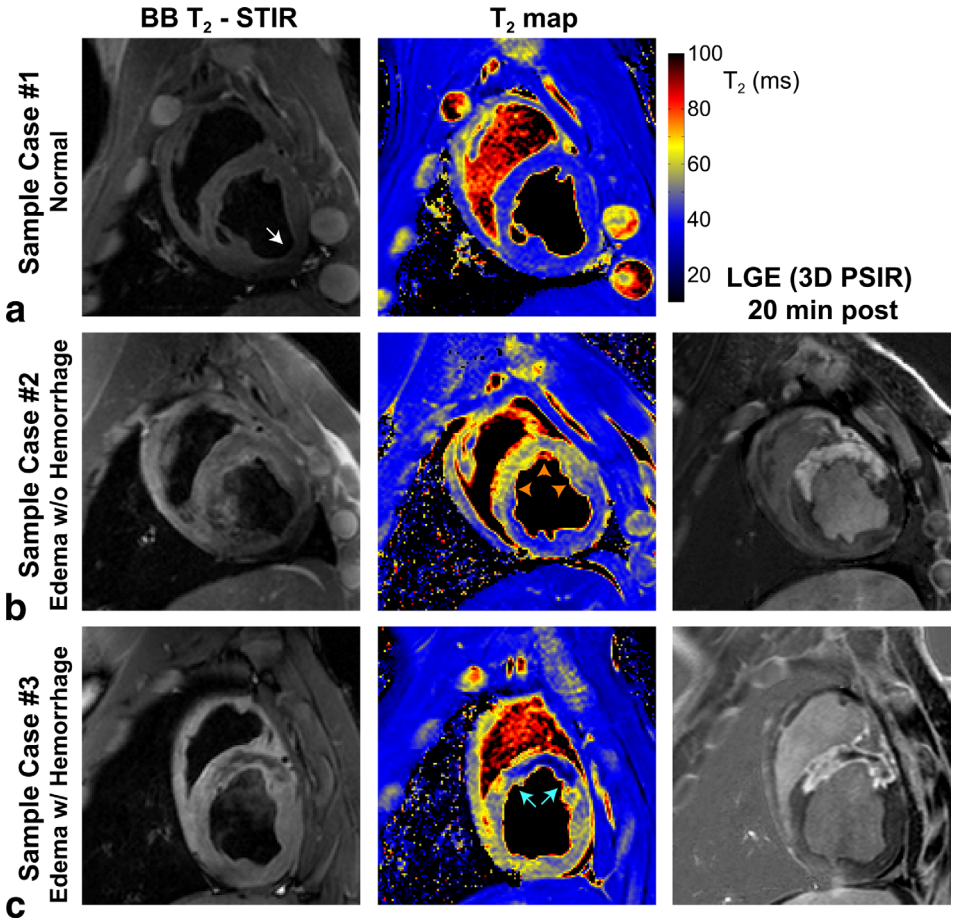

FIG. 6. Comparison of 2D BB T_2-STIR, 3D free breathing T_2 maps, and 3D free breathing phase insensitive inversion recovery (PSIR) LGE from three different swine. Matched slices were chosen manually. **a:** A normal swine displayed homogeneous T_2 values throughout the LV in T_2 map, as expected. However, BB T_2-STIR suffered from signal loss due to motion (white arrow). **b:** The 3 days post-MI swine displayed edema (arrowheads) colocalized with the areas of hyperintensity in LGE. However, BB T_2-STIR failed to display edematous area and was contaminated by the stagnant blood at the endomyocardium of inferolateral wall. Signal loss is observed in the lateral wall as well. **c:** A 3 days post-MI swine displays a distinct hypointense core (arrows) in both the BB T_2-STIR and the T_2 map, though it is easier to appreciate in the T_2 maps. Colocalized area is identified as microvascular obstruction in LGE. The whole ventricle is edematous due to repeated defibrillation during MI induction.

Acquisitions that rely on breath-holding constrain not only the achievable spatial and temporal resolutions and coverage, but also risk scan failure in cases with poor subject compliance. Inter–breath-hold movement or any variability in the breath-hold position will lead to discrepancies in measurements and restrict whole heart evaluations. The use of a navigator-gated acquisition removes constraints on image resolution as demonstrated by the acquisition of whole heart maps with voxel sizes not achievable in a breath-hold or with single-shot imaging. Additionally, motion, variations in heart rate, and T_1 dependency are all major factors that impact the accuracy of T_2 mapping (10,13,26,44,49–51). The proposed method was designed to minimize the effects of these factors on accuracy.

The introduction of SAT prepulse as soon as possible after the QRS complex on the ECG enables efficient scans that utilize every cardiac cycle. Existing techniques, which include multiple T_1 recovery heartbeats during which no imaging is performed, are susceptible to arrhythmias, and can therefore exhibit T_1 dependencies. The "reset" magnetization from every heartbeat provides an ideal baseline for T_2 fitting. T_1 recovery occurs between the SAT pulse and the imaging impacts on the accuracy of the T_2 measurement, which is further reduced by ensuring that constant time between the application of the SAT pulse and the application of the T_2 Prep pulse regardless of RR interval.

The integration of volume interleaving instead of sequential volume acquisition guarantees that any change in physiology is spread over all differentially weighted volumes, further guaranteeing intervolume registration and maintaining excellent pixel-wise fitting. The extension from 2D into 3D, made feasible with navigator gating, not only increases the SNR but also removes any error typically introduced by through-plane motion during breath-holding. No subsampling or acceleration strategies were used in this study to facilitate the measurement of SNR, which resulted in long scan times. Nevertheless, any of the available 3D subsampling strategies is applicable (e.g., 3D-SENSE or 3D-GRAPPA) (21,52). Furthermore, because the multiple volumes

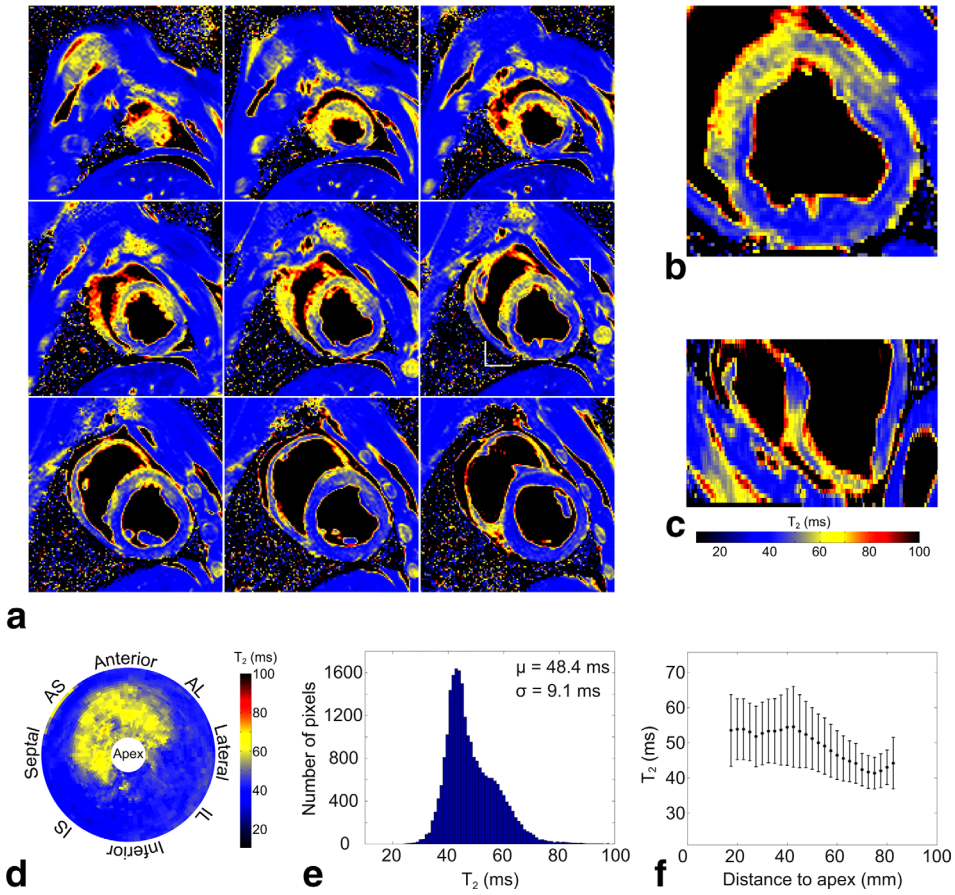

FIG. 7. Representative short axis T_2 maps of an acute MI swine. **a:** Short axis T_2 maps of the whole heart. **b:** Representative magnified short axis slice indicated by the white-cornered inset in panel A. **c:** Reformatted long axis view from the same 3D volume. **d:** Bull's-eye plot reflecting T_2 values through the whole LV and the associated histogram (**e**). **f:** T_2 value distribution over slices. The average coefficient of variation for the multiple slices was 15.7%. AL, anterolateral; AS, anteroseptal; IL, inferolateral; IS, inferoseptal; μ, mean; σ, standard deviation.

acquired are quite similar, it is conceivable that even larger acceleration factors can be achieved using reconstruction techniques that incorporate the parametric maps as final products (53).

This study was preformed at 3T and benefitted from the gain in SNR that was used to achieve higher spatial and temporal resolution. However, the higher field strength also presented challenges due to increased field inhomogeneity and susceptibility artifacts that affect SPGR acquisitions. Hence, the proposed method incorporated the following strategies: 1) a T_2 Prep sequence including adiabatic refocusing pulses made the sequence less affected by B_1+ field inhomogeneity (23); 2) the application of dual-source parallel radiofrequency transmission was used to improve the B_1+ field homogeneity (34,54); 3) SPGR was used instead of bSSFP to prevent banding artifacts due to B_0 field inhomogeneity; and 4) a partial echo readout minimized signal loss due to B_0 field inhomogeneity at susceptibility boundaries.

Other T_2 mapping techniques utilizing differentially T_2-weighted images or volumes have been reported previously, though the majority rely on breath-held 2D acquisitions that have limited in-plane resolution (13,15). van Heeswijk et al. (10) also achieved 3D T_2 maps at 3T using a 3D radial acquisition in combination with golden step-based self-navigation. Using a bSSFP sequence with 20% undersampling resulted in isotropic images (1.7 mm^3). Imaging every other heartbeat recovered SNR, and the residual influence of T_1 was corrected by an empirical factor applied during fitting, which was unnecessary with the technique presented in our study. All data acquired were used, and 3D affine warping of volumes at different respiratory positions was used in final image reconstruction. However, the major difference between van Heeswijk et al.'s technique and the presented 3D T_2 mapping techniques is the use of the SAT pulse. In the present study, the SAT pulse was used to maintain scan efficiency, permitting imaging every heartbeat, and removing the need for postprocessing or registration, as all volumes were interleaved and acquired using the same respiratory navigator and were therefore coregistered. Because no SAT pulse was applied by van Heeswjik et al., increased sensitivity to heart rate variability is expected. In the present study, the positive aspects of using the SAT pulse were offset in part by the expected decreased in SNR of individual volumes. Imaging at 3T using 3D acquisitions was able to restore SNR, resulting in robust and stable measurement of T_2. However, it is likely that in patients with stable heart rhythms, acquisitions utilizing recovery

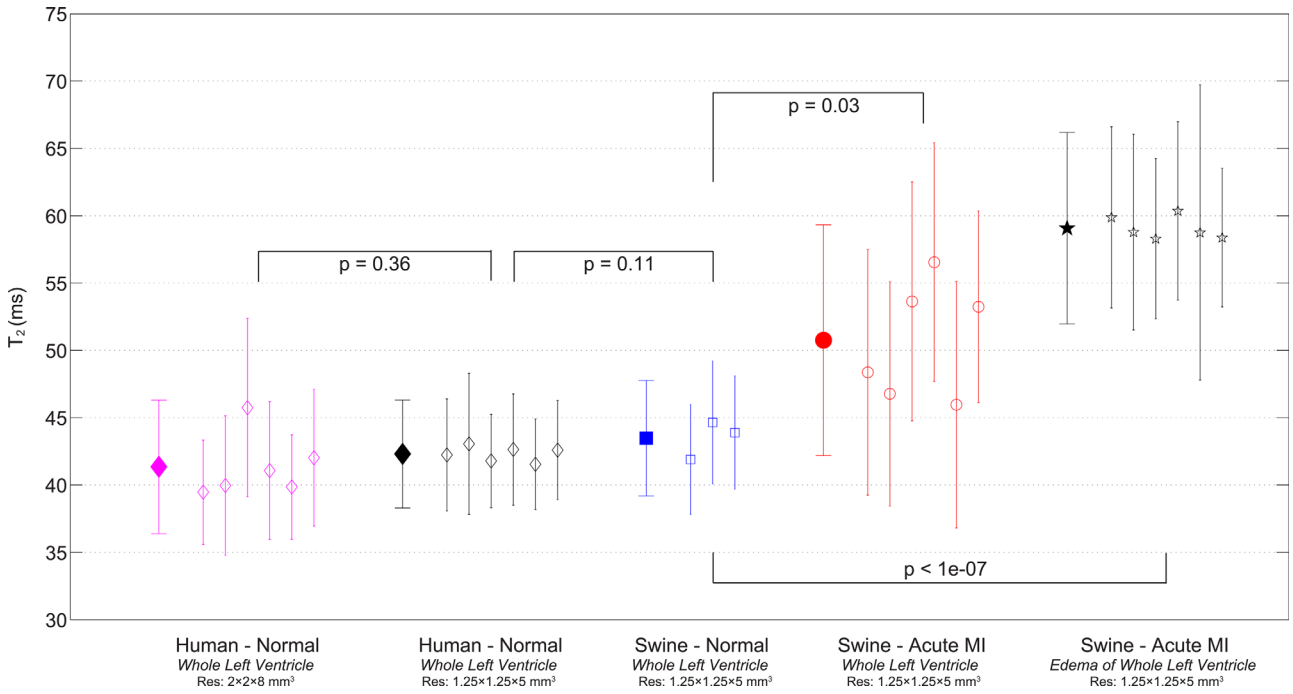

FIG. 8. Comparison of the whole LV T_2 between low imaging resolution in a normal human subject (n = 6, purple diamond) and high imaging resolution in a normal human subject (n = 6, black diamond), normal swine (n = 3, blue square), acute MI swine (n = 6, red circle), and the edema of the whole LV T_2 in acute MI swine (n = 6, black star, imaged 2 to 3 days after MI). Solid symbols denote group averages. Unpaired two-tailed Student's *t* test (Welch's *t* test) results showed significant difference between the average T_2 from normal swine and acute MI swine, as well as the significant difference between the average T_2 from normal swine and edema T_2 from acute MI swine. For the acute MI swine in red, the average T_2 for the whole ventricle included both edematous and normal myocardium.

heartbeats without the use of the SAT preparatory pulse would result in higher SNR efficiency. More work is required to compare the SNR benefits of either approach.

In the present study, the maximum $TE_{T2\,Prep}$ used was 45 ms in vivo and 60 ms for phantoms. Other studies generally have used 55 or 60 ms as a maximum value (10,13,15). Though longer $TE_{T2\,Prep}$ values lead to more T_2-weighting with more signal loss, they also permit more accurate measurement of longer T_2 values in vivo. However, using T_2 Prep risks additional signal loss due to imperfections in refocusing, including those that result from motion. In fact, increasing T_2 Prep significantly could reintroduce the signal loss artifacts that are typical in the BB T_2-STIR sequences that are prevalent in cardiac imaging, since the T_2 Prep is itself a short spin echo sequence that is intolerant to motion. To avoid signal loss due to motion, both T_2 Prep and imaging should be placed in diastasis, which can be difficult for high heart rates or for very long $TE_{T2\,Prep}$ values.

The whole heart T_2 maps did not show significant fluctuation among slabs in normal hearts (Fig. 9). The average T_2 value of the apical regions was not significantly different from that of the other slices. Though no significant difference was found between low-resolution and high-resolution acquisitions, the CVs and measurement standard deviations did decrease with higher-resolution imaging, implying that increases in resolution can improve the stability of T_2 measurements. A reduction in partial volume effects and reduced sensitivity to motion may explain this improvement over previous studies (10,13,17,36).

The measurement of T_2 was consistent enough between animals or between human subjects, which made it possible to determine a reference T_2 threshold that could be used for segmentation of edematous areas in swine with acute MI. This implies that no reference tissue in the images themselves is needed, as is the case in most analysis of BB T_2-STIR images. Furthermore, having a standard threshold for segmentation that is independent of the acquired images made possible the identification of edematous regions in hearts that had globally elevated T_2 due to repeated defibrillation during reperfusion (Fig. 6C).

In the acute stages, MI presents with complex pathophysiological processes such as tissue edema, necrosis, hemorrhage, microvascular obstruction, and fibrosis. The proposed technique is sensitive and accurate enough to distinguish edema from normal myocardium, though more work is needed to confirm the accurate visualization of hemorrhage. Nevertheless, the proposed technique demonstrates that T_2 measurement can be a sensitive probe for this complicated process; the accurate and quantitative nature of 3D T_2 mapping make it a great candidate for future use in in vivo studies to explore the wound healing process, assess novel therapies, and risk stratify patient post MI.

Limitations

The 3D T_2 maps presented here were calculated from fully sampled acquisitions of three or four T_2-weighted volumes. Although 3D acquisitions require significantly longer scan times which are not amenable to single-shot

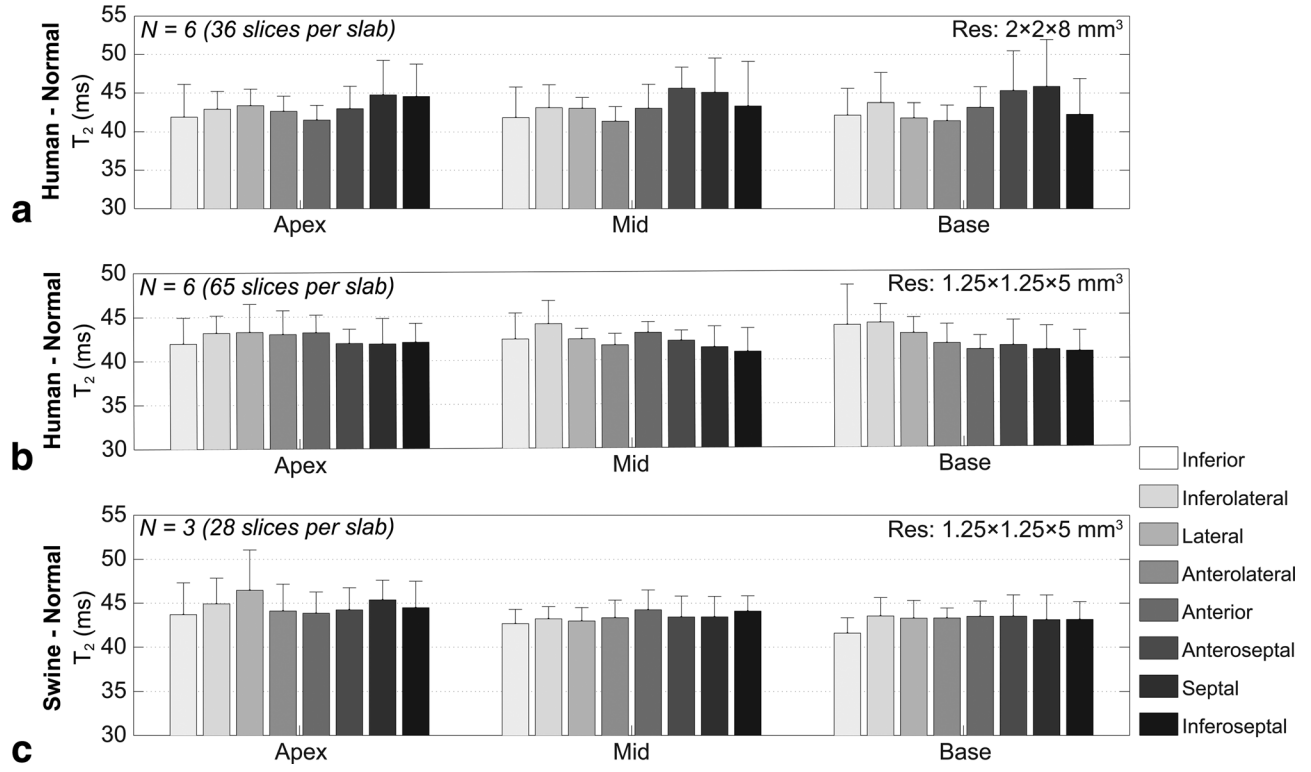

FIG. 9. T_2 distribution over whole LV from apex to base and around the hearts from inferior to inferoseptal (eight radial segments per slab and apex-mid-base slab distributions). T_2 values varied more in the low-resolution normal human subjects than in the high-resolution normal human subjects, which may be due to a greater partial volume effect in the low-resolution images.

acquisitions, k-space segmentation permits much higher temporal and spatial resolution, producing higher-quality parametric maps with low CVs. The averaged prescribed scan time for three low-resolution volumes ($2 \times 2 \times 8$ mm^3) and four high-resolution volumes ($1.25 \times 1.25 \times 5$ mm^3) with a field of view of approximately $270 \times 230 \times 90$ mm^3 was 2.2 min and 8.9 min, respectively. The long scan times used in this study may present a barrier to the use of the proposed technique in a routine clinical examination. However, no acceleration in the form of parallel imaging was used to facilitate accurate measurement of SNR. There is no reason to believe that standard parallel imaging or the current state-of-the-art acceleration strategies such as k-t FOCUSS (55) or compressed sensing in parameter mapping could not be applied (53,56).

The nonselective SAT prepulse used in this study was not insensitive to B_1+ field inhomogeneity, which could result in compromised T_2 measurement accuracy for tissues with longer T_2 values, and increase measurement sensitivity to arrhythmias via residual unsuppressed signal (57). Similarly, the rectangular nonselective 90° tip up/down pulses used as part of T_2 Prep could lead to imperfect magnetization preparation and errors in T_2 measurement, since the non–T_2-prepared volume is imaged with full magnetization. The use of ROI-specific B_1+ field shimming was helpful in reducing this possible source of error (34), as reflected by the good correlation with gold standard measures as well as the high R^2 values, though these radiofrequency pulses should certainly be improved in future work or for cases in which B_1+ shimming is not available.

The shortest $TE_{T2\,Prep}$ used in this study was 25 ms, which is limited by the current system and the choice of standard adiabatic pulses for refocusing. The performance of the sequence could likely be improved by using shorter adiabatic pulses (at the expense of B_1+ homogeneity) that would in turn permit better distribution of the $TE_{T2\,Prep}$ values and better sampling of the T_2 decay curve of short T_2 species. Further exploration is needed.

CONCLUSION

In this study, we present a novel and robust 3D free-breathing T_2 mapping sequence that achieves whole heart coverage with a high degree of homogeneity. The sequence takes advantage of the higher SNR available at 3T and uses SPGR to reduce sensitivity to field inhomogeneity. A SAT prepulse is used to decrease sensitivity to heart rate variability and arrhythmias, and volume-interleaved acquisitions remove issues of misregistration between the multiple volumes used in the voxel-wise calculation of T_2. High spatial resolution T_2 maps acquired during free breathing are demonstrated in normal human subjects as well as in swine with acute myocardial infarction.

The proposed sequence enables the use of quantitative metrics in the detection and assessment of acute myocardial injury and should provide a tool for the assessment of the area at risk. Relative to conventional T_2-weighted spin-echo imaging currently used in myocardial edema detection, quantitative T_2 mapping provides a promising alternative. Further studies on reproducibility and the

pathological evolution of acute injury may be needed to best deploy this quantitative technique.

APPENDIX 1

Calculation of T_2 Maps

Parametric maps were calculated using linear regression of the log-transformed data as applied to the $n \in 1 \ldots N_{vol}$ differently T_2-weighted volumes. Two parameters (A_0 and T_2) were fit using the following relationship, which assumes that for a given voxel the magnetization at the start of imaging is a function of T_1 and T_{SAT}, and an additional exponential term introduced by the T_2 decay that occurred during T_2 Prep:

$$S_n = A_0(T_{SAT}, T_1) \cdot e^{-\frac{TE_{T_2Prep,n}}{T_2}}. \quad [A1]$$

Here, S_n is signal intensity in a given voxel for the n^{th} differentially T_2-weighted volume; $A_0(T_{SAT}, T_1)$ is the signal available right before T_2 Prep and is a function of both T_1 and the available time for recovery T_{SAT}, which is a function of heart rate; and $TE_{T2\ Prep,n}$ is the echo time for the n^{th} T_2 Prep. A_0 is defined as $A_0 = 1 - e^{-\frac{T_{SAT}}{T_1}}$, which assumes perfect saturation, but can also include the residual effects of imperfect saturation. After log transformation, the relationship becomes

$$\ln[S_n] = \ln[A_0(T_{SAT}, T_1)] - \left[\frac{TE_{T_2Prep,n}}{T_2}\right]. \quad [A2]$$

The closed form solutions for the coefficients of the linear regression of the form $y = B_1X + B_0$ are given by

$$B_1 = \frac{\sum_{n=1}^{N_{vol}}(x_n - \bar{x}) \cdot y_n}{\sum_{n=1}^{N_{vol}}(x_n - \bar{x})^2} \quad [A3]$$

$$B_0 = \bar{y} - B_1 \cdot \bar{x}, \quad [A4]$$

where $\bar{x}$ and $\bar{y}$ represent the means of x and y, respectively, and $T_2 = -\frac{1}{B_1}$ and $A_0 = e^{B_0}$. To guarantee the displayed data had a good fit to the model, all the pixels with $R^2 < 0.9$ (the residual sum of squares from the linear regression) were excluded from display in the parametric maps. R^2 was calculated as

$$R^2 = \frac{\left[\sum_n x_n y_n - \frac{\sum_n x_n \cdot \sum_n y_n}{N_{vol}}\right]^2}{\left[\sum_n x_n^2 - \frac{\left(\sum_n x_n\right)^2}{N_{vol}}\right] \cdot \left[\sum_n y_n^2 - \frac{\left(\sum_n x_n\right)^2}{N_{vol}}\right]}. \quad [A5]$$

APPENDIX 2

Calculation of Heart Rate–Related Trigger Delay

Here the heart-related middiastolic imaging trigger delay is calculated from an empirical equation (24). The duration of systole T_{sys} is

$$T_{sys} = k_1 \cdot \log[10 \cdot (T_{RR} + k_2)], \quad [A6]$$

where k_1 is 0.375 for young men and children, 0.385 for women aged 15–32 years, 0.380 for men aged >45 years, and 0.390 for women aged >45 years, and k_2 is 0.07 (24,35). In this study, $k_1 = 0.385$ and $k_2 = 0.07$ were used in simulations. T_{RR} represents the time between subsequent R waves of the ECG or the RR interval of each heartbeat cycle.

The corresponding duration of diastole T_{dias} is:

$$T_{dias} = T_{RR} - T_{sys} = T_{RR} - k_1 \cdot \log[10 \cdot (T_{RR} + k_2)]. \quad [A7]$$

The middiastolic trigger delay $T_{mid-dias}$ is given by

$$T_{mid-dias} = T_{sys} + \frac{T_{dias}}{2}. \quad [A8]$$

REFERENCES

1. Abdel-Aty H, Boye P, Zagrosek A, Wassmuth R, Kumar A, Messroghli D, Bock P, Dietz R, Friedrich MG, Schulz-Menger J. Diagnostic performance of cardiovascular magnetic resonance in patients with suspected acute myocarditis: comparison of different approaches. J Am Coll Cardiol 2005;45:1815–1822.
2. Vignaux O, Dhote R, Duboc D, Blanche P, Devaux JY, Weber S, Legmann P. Detection of myocardial involvement in patients with sarcoidosis applying T2-weighted, contrast-enhanced, and cine magnetic resonance imaging: initial results of a prospective study. J Comput Assist Tomogr 2002;26:762–767.
3. Joshi SB, Chao T, Herzka DA, Zeman PR, Cooper HA, Lindsay J, Fuisz AR. Cardiovascular magnetic resonance T2 signal abnormalities in left ventricular ballooning syndrome. Int J Cardiovasc Imaging 2010;26:227–232.
4. Arai AE, Leung S, Kellman P. Controversies in cardiovascular MR imaging: reasons why imaging myocardial T2 has clinical and pathophysiologic value in acute myocardial infarction. Radiology 2012;265:23–32.
5. Schwitter J, Arai AE. Assessment of cardiac ischaemia and viability: role of cardiovascular magnetic resonance. Eur Heart J 2011;32:799–809.
6. Friedrich MG. Myocardial edema—a new clinical entity? Nat Rev Cardiol 2010;7:292–296.
7. Aletras AH, Tilak GS, Natanzon A, Hsu LY, Gonzalez FM, Hoyt RF Jr, Arai AE. Retrospective determination of the area at risk for reperfused acute myocardial infarction with T2-weighted cardiac magnetic resonance imaging: histopathological and displacement encoding with stimulated echoes (DENSE) functional validations. Circulation 2006;113:1865–1870.
8. Abdel-Aty H, Simonetti O, Friedrich MG. T2-weighted cardiovascular magnetic resonance imaging. J Magn Reson Imaging 2007;26:452–459.
9. Butler CR, Thompson R, Haykowsky M, Toma M, Paterson I. Cardiovascular magnetic resonance in the diagnosis of acute heart transplant rejection: a review. J Cardiovasc Magn Reson 2009;11:7.
10. van Heeswijk RB, Piccini D, Feliciano H, Hullin R, Schwitter J, Stuber M. Self-navigated isotropic three-dimensional cardiac T2 mapping. Magn Reson Med 2015;73:1549–1554.
11. Simonetti OP, Finn JP, White RD, Laub G, Henry DA. "Black blood" T2-weighted inversion-recovery MR imaging of the heart. Radiology 1996;199:49–57.
12. Kellman P, Aletras AH, Mancini C, McVeigh ER, Arai AE. T2-prepared SSFP improves diagnostic confidence in edema imaging in acute myocardial infarction compared to turbo spin echo. Magn Reson Med 2007;57:891–897.
13. Giri S, Chung YC, Merchant A, Mihai G, Rajagopalan S, Raman SV, Simonetti OP. T2 quantification for improved detection of myocardial edema. J Cardiovasc Magn Reson 2009;11:56.
14. Salerno M, Kramer CM. Advances in parametric mapping with CMR imaging. JACC Cardiovasc Imaging 2013;6:806–822.
15. Verhaert D, Thavendiranathan P, Giri S, Mihai G, Rajagopalan S, Simonetti OP, Raman SV. Direct T2 quantification of myocardial edema in acute ischemic injury. JACC Cardiovasc Imaging 2011;4:269–278.
16. Usman AA, Taimen K, Wasielewski M, et al. Cardiac magnetic resonance T2 mapping in the monitoring and follow-up of acute cardiac transplant rejection: a pilot study. Circ Cardiovasc Imaging 2012;5:782–790.
17. Thavendiranathan P, Walls M, Giri S, Verhaert D, Rajagopalan S, Moore S, Simonetti OP, Raman SV. Improved detection of myocardial

involvement in acute inflammatory cardiomyopathies using T2 mapping. Circ Cardiovasc Imaging 2012;5:102–110.
18. Ghugre NR, Ramanan V, Pop M, Yang Y, Barry J, Qiang B, Connelly KA, Dick AJ, Wright GA. Myocardial BOLD imaging at 3 T using quantitative T2: application in a myocardial infarct model. Magn Reson Med 2011;66:1739–1747.
19. Ugander M, Bagi PS, Oki AJ, Chen B, Hsu LY, Aletras AH, Shah S, Greiser A, Kellman P, Arai AE. Myocardial edema as detected by precontrast T1 and T2 CMR delineates area at risk associated with acute myocardial infarction. JACC Cardiovasc Imaging 2012;5:596–603.
20. Wassmuth R, Prothmann M, Utz W, Dieringer M, von Knobelsdorff-Brenkenhoff F, Greiser A, Schulz-Menger J. Variability and homogeneity of cardiovascular magnetic resonance myocardial T2-mapping in volunteers compared to patients with edema. J Cardiovasc Magn Reson 2013;15:27.
21. Weiger M, Pruessmann KP, Boesiger P. 2D SENSE for faster 3D MRI. MAGMA 2002;14:10–19.
22. Brittain JH, Hu BS, Wright GA, Meyer CH, Macovski A, Nishimura DG. Coronary angiography with magnetization-prepared T2 contrast. Magn Reson Med 1995;33:689–696.
23. Nezafat R, Stuber M, Ouwerkerk R, Gharib AM, Desai MY, Pettigrew RI. B1-insensitive T2 preparation for improved coronary magnetic resonance angiography at 3 T. Magn Reson Med 2006;55:858–864.
24. Roes SD, Korosoglou G, Schar M, Westenberg JJ, van Osch MJ, de Roos A, Stuber M. Correction for heart rate variability during 3D whole heart MR coronary angiography. J Magn Reson Imaging 2008; 27:1046–1053.
25. Wang Y, Rossman PJ, Grimm RC, Riederer SJ, Ehman RL. Navigator-echo-based real-time respiratory gating and triggering for reduction of respiration effects in three-dimensional coronary MR angiography. Radiology 1996;198:55–60.
26. Giri S, Shah S, Xue H, Chung Y-C, Pennell ML, Guehring J, Zuehlsdorff S, Raman SV, Simonetti OP. Myocardial T2 mapping with respiratory navigator and automatic nonrigid motion correction. Magn Reson Med 2012;68:1570–1578.
27. Xue H, Shah S, Greiser A, Guetter C, Littmann A, Jolly MP, Arai AE, Zuehlsdorff S, Guehring J, Kellman P. Motion correction for myocardial T1 mapping using image registration with synthetic image estimation. Magn Reson Med 2012;67:1644–1655.
28. Weingartner S, Akcakaya M, Roujol S, Basha T, Stehning C, Kissinger KV, Goddu B, Berg S, Manning WJ, Nezafat R. Free-breathing post-contrast three-dimensional T1 mapping: Volumetric assessment of myocardial T1 values. Magn Reson Med 2014. doi: 10.1002/mrm.25124.
29. Andia ME, Henningsson M, Hussain T, Phinikaridou A, Protti A, Greil G, Botnar RM. Flow-independent 3D whole-heart vessel wall imaging using an interleaved T2-preparation acquisition. Magn Reson Med 2013;69:150–157.
30. Wilman AH, Riederer SJ, King BF, Debbins JP, Rossman PJ, Ehman RL. Fluoroscopically triggered contrast-enhanced three-dimensional MR angiography with elliptical centric view order: application to the renal arteries. Radiology 1997;205:137–146.
31. Huang F, Lin W, Li Y. Partial fourier reconstruction through data fitting and convolution in k-space. Magn Reson Med 2009;62:1261–1269.
32. Johnson K, Patel S, Whigham A, Hakim A, Pettigrew R, Oshinski J. Three-dimensional, time-resolved motion of the coronary arteries. J Cardiovasc Magn Reson 2004;6:663–673.
33. Schär M, Vonken EJ, Stuber M. Simultaneous B0- and B1+-map acquisition for fast localized shim, frequency, and RF power determination in the heart at 3 T. Magn Reson Med 2010;63:419–426.
34. Herzka DA, Ding H, Schär M. Improvement in B1+ Homogeneity of 3T Cardiac MRI in Swine with Dual-Source Parallel RF Excitation. In Proceedings of the 21st Annual Meeting of ISMRM, Salt Lake City, Utah, USA, 2013. p. 72.
35. Ashman R, Hull E. The normal human electrocardiogram and changes produced by disease. The T wave, the Q-T interval, and the U wave. In: Essentials of electrocardiography: for the student and practitioner of medicine, 2nd edition. New York: Macmillan; 1945. p 162–163.
36. von Knobelsdorff-Brenkenhoff F, Prothmann M, Dieringer MA, Wassmuth R, Greiser A, Schwenke C, Niendorf T, Schulz-Menger J. Myocardial T1 and T2 mapping at 3 T: reference values, influencing factors and implications. J Cardiovasc Magn Reson 2013;15:53.
37. Look DC. Time saving in measurement of NMR and EPR relaxation times. Rev Sci Instrum 1970;41:250.
38. Sasano T, McDonald AD, Kikuchi K, Donahue JK. Molecular ablation of ventricular tachycardia after myocardial infarction. Nat Med 2006; 12:1256–1258.
39. Kellman P, Arai AE, McVeigh ER, Aletras AH. Phase-sensitive inversion recovery for detecting myocardial infarction using gadolinium-delayed hyperenhancement. Magn Reson Med 2002;47:372–383.
40. Lee S, Schär M, Zviman M, Sena-Weltin V, Harouni A, Kozerke S, McVeigh E, Halperin H, Herzka D. Free breathing independent respiratory navigator-gated imaging: concurrent PSIR and T2-weighted 3D imaging of the left ventricle. In Proceedings of the 19th Annual Meeting of ISMRM, Montreal, Canada, 2011. p 19.
41. Scientific Computing and Imaging Institute (SCI). "Seg3D" Volumetric image segmentation and visualization. Version 2.1.4. http://www.sci.utah.edu/cibc-software/seg3d.html. Updated February 24, 2012. Accessed August 10, 2012.
42. Borland D, Taylor MR 2nd. Rainbow color map (still) considered harmful. IEEE Comput Graph Appl 2007;27:14–17.
43. Cerqueira MD. Standardized myocardial segmentation and nomenclature for tomographic imaging of the heart: a statement for healthcare professionals from the cardiac imaging committee of the council on clinical cardiology of the american heart association. Circulation 2002;105:539–542.
44. van Heeswijk RB, Feliciano H, Bongard C, Bonanno G, Coppo S, Lauriers N, Locca D, Schwitter J, Stuber M. Free-breathing 3 T magnetic resonance T2-mapping of the heart. JACC Cardiovasc Imaging 2012;5:1231–1239.
45. Guo H, Au WY, Cheung JS, et al. Myocardial T2 quantitation in patients with iron overload at 3 Tesla. J Magn Reson Imaging 2009; 30:394–400.
46. Wu KC. CMR of microvascular obstruction and hemorrhage in myocardial infarction. J Cardiovasc Magn Reson 2012;14:68.
47. Lotan CS, Bouchard A, Cranney GB, Bishop SP, Pohost GM. Assessment of postreperfusion myocardial hemorrhage using proton NMR imaging at 1.5 T. Circulation 1992;86:1018–1025.
48. Ghugre NR, Ramanan V, Pop M, Yang Y, Barry J, Qiang B, Connelly KA, Dick AJ, Wright GA. Quantitative tracking of edema, hemorrhage, and microvascular obstruction in subacute myocardial infarction in a porcine model by MRI. Magn Reson Med 2011;66:1129–1141.
49. Foltz WD, Al-Kwifi O, Sussman MS, Stainsby JA, Wright GA. Optimized spiral imaging for measurement of myocardial T2 relaxation. Magn Reson Med 2003;49:1089–1097.
50. Huang TY, Liu YJ, Stemmer A, Poncelet BP. T2 measurement of the human myocardium using a T2-prepared transient-state TrueFISP sequence. Magn Reson Med 2007;57:960–966.
51. Blume U, Lockie T, Stehning C, Sinclair S, Uribe S, Razavi R, Schaeffter T. Interleaved T1 and T2 relaxation time mapping for cardiac applications. J Magn Reson Imaging 2009;29:480–487.
52. Blaimer M, Breuer FA, Mueller M, Seiberlich N, Ebel D, Heidemann RM, Griswold MA, Jakob PM. 2D-GRAPPA-operator for faster 3D parallel MRI. Magn Reson Med 2006;56:1359–1364.
53. Doneva M, Bornert P, Eggers H, Stehning C, Senegas J, Mertins A. Compressed sensing reconstruction for magnetic resonance parameter mapping. Magn Reson Med 2010;64:1114–1120.
54. Mueller A, Kouwenhoven M, Naehle CP, Gieseke J, Strach K, Willinek WA, Schild HH, Thomas D. Dual-source radiofrequency transmission with patient-adaptive local radiofrequency shimming for 3.0-T cardiac MR imaging: initial experience. Radiology 2012;263: 77–85.
55. Feng L, Otazo R, Jung H, Jensen JH, Ye JC, Sodickson DK, Kim D. Accelerated cardiac T2 mapping using breath-hold multiecho fast spin-echo pulse sequence with k-t FOCUSS. Magn Reson Med 2011; 65:1661–1669.
56. Huang C, Graff CG, Clarkson EW, Bilgin A, Altbach MI. T2 mapping from highly undersampled data by reconstruction of principal component coefficient maps using compressed sensing. Magn Reson Med 2012;67:1355–1366.
57. Kim D, Gonen O, Oesingmann N, Axel L. Comparison of the effectiveness of saturation pulses in the heart at 3T. Magn Reson Med 2008;59:209–215.